The golden ark: Arsenopyrite crystal plasticity and the retention of gold through high strain and metamorphism.

Denis Fougerouse[1,2], Steven Micklethwaite[2,3], Angela Halfpenny[4,5], Steven Reddy[1], John B. Cliff[6], Laure A.J. Martin[6], Matt Kilburn[6], Paul Guagliardo[6], and Stanislav Ulrich[7]

[1]Department of Applied Geology, Curtin University, GPO Box U1987, Perth, WA 6845, Australia

[2]Centre for Exploration Targeting, School of Earth and Environment, The University of Western Australia, M006, 35 Stirling Highway, Crawley, WA 6009, Australia

[3]School of Earth, Atmosphere & Environment, Monash University, Melbourne, Victoria, Australia

[4]Microscopy & Microanalysis Facility, John de Later Centre, Curtin University, GPO BOX U1987, Perth, WA 6845, Australia

[5]CSIRO Earth Science and Resource Engineering, Minerals Down Under Flagship, ARRC, 26 Dick Perry Avenue, Kensington, WA 6151, Australia

[6]Centre for Microscopy, Characterisation and Analysis, The University of Western Australia, 35 Stirling Highway, Crawley, WA 6009, Australia

[7]AngloGold Ashanti Ltd, Asset Development, 44 St George Terrace, Perth, WA 6000, Australia

ABSTRACT

Quantitative electron backscatter diffraction analysis and ion microprobe imaging of gold-rich arsenopyrites provide the first insights into the crystal plasticity and element mobility behaviour of arsenopyrites through metamorphism (340° - 460° and 2 kbars). Remarkably, the gold-rich arsenopyrites remained structurally and chemically robust during high strain deformation. It is only during a superimposed lower strain deformation event, at a high angle

to the preferred orientation of the arsenopyrites, that small amounts of crystal plasticity affected the arsenopyrites. During the low strain event a dissolution-reprecipitation reaction resulted in loss of gold from the crystal lattice, facilitated by localised domains of recrystallization, most likely due to fluid percolation along sub- and new grain boundaries. We suggest the abundance and rheologically robust nature of gold-rich arsenopyrite in giant gold deposits, affected by greenschist-amphibolite metamorphism, is actually a critical factor in the preservation of those deposits.

INTRODUCTION

Although rarely acknowledged, arsenopyrite is one of the world's most important sulphide minerals. It is ubiquitous as a gold bearing phase in many giant deposits, particularly in sediment hosted orogenic gold deposits (Groves et al., 1998) as documented at Obuasi, Ghana, (Oberthür et al., 1994), Sunrise Dam, Australia (Sung et al., 2009), Muruntau, Uzbekistan (Morelli et al., 2007) or Red Lake, Canada (Dubé et al., 2004). The presence of arsenic and arsenopyrite also provide important vectors to mineral resources (Boyle and Jonasson, 1973; Eilu and Groves, 2001; Le Vaillant et al., 2015). For these reasons it is surprising that almost nothing is known about the crystal plasticity of arsenopyrite, nor the influence of microstructure on the ability of arsenopyrite to retain or release its major and trace element content.

In contrast to arsenopyrite, the crystal plasticity of other sulphide phases such as pyrite, pyrrhotite, sphalerite, chalcopyrite, galena, stibnite and pentlandite have been investigated in detail (Barrie et al., 2011; Boyle et al., 1998; Cox, 1987; Kelly and Clark, 1975; Vukmanovic et al., 2014). These studies conclude that crystal plasticity of phases, such as pyrite, occurs relatively easily at temperatures as low as 260 °C and strain rates of approximately 10^{-12} - 10^{-}

^{16} s^{-1} (Barrie et al., 2011) and can have a significant impact on trace element mobility (Reddy and Hough, 2013).

Here we provide the first documentation of arsenopyrite crystal plastic behaviour under high strain and greenshist facies metamorphic conditions. We examine the impact on trace element modification, with important implications for both resource preservation and the release of elements from arsenopyrite back to the natural environment.

SAMPLES AND METHODS

In order to examine the crystal-plastic behaviour of arsenopyrite and its impact on trace element mobility, arsenopyrites with large enrichments of trace elements (Au, Ni) and well-constrained metamorphic-strain conditions were selected from the economic refractory ores of the giant Obuasi deposit. The mineralized arsenopyrites are hosted in paleoproterozoic sheared phyllites (2155 Ma, zircon U/Pb maximum age of deposition; Oberthür et al., 1998) composed of micas, quartz, carbonates (ankerite and siderite), chlorites, rutile and graphite. Arsenopyrite growth and mineralization occurred during continuous cleavage development and peak upper greenschist metamorphism at 340° - 460° and 2 kbars as shown by the development of strain shadows parallel with the continuous cleavage surrounding the arsenopyrites (the Eburnean orogeny: Schwartz et al. 1992; Oberthür et al. 1994; Fougerouse et al. in press). A large sample suite (>200 samples) was collected and studied from mineralised exposures of the Obuasi mine to provide representative petrographical and geochemical results across the deposit. Two grains from sample 215-20 are reported in this study, collected ~950 m below the surface from a 10 m wide high strain domain associated with thick quartz veins, between two graphitic shear zones. The arsenopyrites have been subject to two strain events (Fougerouse et al., in press-b), mostly accommodating pure shear. The first event is high strain, at the peak of metamorphism, which occurred during the Eburnean orogeny ($D2_{Ob}$; Fougerouse et al., in press). A pervasive

continuous cleavage developed while the quartz veins underwent boudinage and strain shadows developed around the arsenopyrite grains (Fig. 1). The long-axes of the acicular arsenopyrites (up to 0.1x1 mm) are aligned parallel to the cleavage. A large minimum finite strain of 48% shortening and 235% stretch, perpendicular to the shortening, was estimated for the hosting phyllites from strain shadow length and fold periodicity (Fig. 1; p. 271 Ramsay and Huber, 1983), using oriented thin sections cut orthogonal to the cleavage and parallel to the lineation. Nonetheless, the arsenopyrite grains themselves remain largely euhedral and relatively undeformed (Fig. 2). In the second event ($D3_{Ob}$), a low strain overprinting crenulation cleavage developed, representing a minimum shortening estimated at 15% with no associated stretch. The long-axes of the arsenopyrites are oriented at a high angle to the later crenulation cleavage.

Backscattered Scanning Electron Microscopy imaging (BSE) and Secondary Ion Mass Spectrometer (SIMS and NanoSIMS) investigations were carried out at the Centre for Microscopy, Characterisation and Analysis, University of Western Australia. BSE images were collected using a TESCAN VEGA3 SEM and large area ion imaging of ^{197}Au were performed on a Cameca IMS 1280 ion probe on 150x150 micron areas using a ~1 micron, Cs^+ primary beam. Ions were collected in peak-hopping mode in an ion-counting electron multiplier at a mass resolution of ~3000. High-resolution elemental mapping was carried out using the Cameca NanoSIMS 50 with a spot size of approximately 100 nm and a Cs^+ primary beam. The experiment allowed simultaneous detection of ^{197}Au and ^{34}S across areas measuring 100 x 100 μm with a 120 nm/pixel resolution. Quantitative orientation maps of arsenopyrite crystal lattice were recorded using EBSD (Prior et al., 1999) at the CSIRO Earth Science and Resource Engineering in Kensington (Australia) using a Zeiss Ultraplus FEG SEM and at Curtin University using a TESCAN MIRA3 SEM. Systematic mis-indexing due to pseudosymmetry within the arsenopyrite grains was removed by identifying the axis and angle relationships to rotate the points and produce a correctly indexed grain. It should be noted that pseudosymmetry

is a problem in pyrite and arsenopyrite. Correcting for pseudosymmetry can produce internally consistent datasets, although the actual solution may still be wrong (Nolze et al., 2016), however in this study such issues do not change our conclusions.

RESULTS

Arsenopyrites from the ore zone of the Obuasi deposit are composed of two primary domains: rims that appear homogenous in BSE images (A-rims) and inclusion-rich internal cores. The cores contain inclusions of pyrrhotite, chalcopyrite or rutile. There is then a discontinuously developed third domain (B-rims) crosscutting all others (Fig. 3). B-rims are characterised by higher arsenic concentrations (~46 wt% as opposed to ~44 wt% in A-rims; Fougerouse et al. in press) and preserve the original shape of the crystals. The B-rim contacts are sharp, planar to curvilinear (bulbous) and penetrate in from microcracks and grain boundaries (Fig. 3).

The EBSD data show a relative change in crystallographic orientation for each grain (Fig. 2 and 3). Consistent with other studies investigating sulphides crystal-plasticity (Reddy and Hough 2013), we define high-angle grain boundaries to have misorientations ≥10°. All boundaries <10° are low-angle grain boundaries, representing subgrains. In most cases the intragrain variation does not reach 5°, though new grains are formed at a few localised points.

The analysis reveals a difference in the deformation intensity between grain 1 and 2 (Figs. 2 and 3). Grain 1 is parallel to the main cleavage ($S2_{Ob}$), in a domain unaffected by the later crenulation cleavage ($S3_{Ob}$), and contains only weak internal deformation (maximum of 3° misorientation). Conversely, grain 2 is located on a fold flexure of the $S3_{Ob}$ crenulation. In this crystal, high densities of misorientations occur in a narrow localised domain, adjacent to a fracture filled with pyrite (Fig. 3D). In this domain, the misorientations define low- and high-angle boundaries creating new small sized grains. In the centre top of the grain an incipient

domain of less than 3° misorientation is developed. The cumulative orientation profiles (Fig. 3H) along the short axis of grain 2 show minor misorientations (<2°), but much greater misorientations are achieved parallel to the long axis of the arsenopyrite (up to 7° from the tip of the grain to the core). Pole figure data indicates a dispersion of the orientation (Fig. 3). In addition, the pyrite crystal infilling the fracture of grain 2 is virtually undeformed (misorientation up to 2°; Fig. 3C).

The SIMS and NanoSIMS ^{197}Au ion microprobe imaging reveals that the distribution of the gold is zoned within the crystals, with gold-rich A-rims around gold-poor cores (Fig. 2 and 3). The A-rims are in turn crosscut by gold-poor B-rims (Fig. 3F). The A-rims represent epitaxial zones with up to 1000 ppm Au (Fisher et al., 2014; Oberthür et al., 1994), although these concentrations decrease on the outer edges of the grain as shown on the left side of grain 2 (Fig. 3). An A-rim is well developed in grain 1 where minimal internal deformation occurred. In grain 2, a large A-rim is cut by discontinuous B-rims, characterized by low Au signal. Internally, the A-rims are finely zoned with submicron-scale concentric bands with sharp boundaries (Fig. 3F; Fougerouse et al. in press GCA). However, this fine epitaxial zoning in the domain of high misorientation identified in grain 2, appears blurry, with diffuse boundaries between bands and locally, small spherical high Au concentrations. The fuzzy gold signal in this domain is also dissected by numerous small scale, sharply defined B-rims with low Au signals. Critically, the overall B-rim width in this region of high densities of misorientations is up to three times greater in comparison with the domains of undeformed arsenopyrite.

CRYSTAL-PLASTIC EVOLUTION OF ARSENOPYRITES AND CONSEQUENCES FOR GOLD RETENTION

The crystallographic misorientations and localised intragrain textures, revealed by EBSD, are consistent with dynamic recrystallisation by dislocation creep (Hirth and Tullis, 1992; Urai

et al., 1986). In grain 2, this led to the development of subgrains and neoblasts accommodating crystal-plastic strain in a narrow localised domain, on the top right-hand side of the crystal. This crystal-plastic strain domain is coincident with a fracture filled with undeformed pyrite (Fig. 1). Overall, several significant features emerge from our analysis.

Firstly, grain 1 and grain 2 formed during high strain ($D2_{Ob}$, 50% flattening, >200% stretch) and upper greenschist metamorphism (John et al., 1999; Schwartz et al., 1992), then were subject to a second shortening event ($D3_{Ob}$, ~15% shortening), yet remained euhedral and underwent only minor crystal-plastic deformation. Secondly, grain 1 has minimal lattice distortion (≤3° of misorientation from grain tip to centre) in comparison to grain 2, which contains a localized domain of subgrains, neoblasts and microfracture. In this regard, grain 1 is located parallel to the $S2_{Ob}$ cleavage, in a microlithon between two crenulation planes ($S3_{Ob}$), while grain 2 is located on a fold flexure of the $S3_{Ob}$ cleavage. These relationships indicate that crystal plastic microstructures developed not during the high strain peak metamorphic event but during microfolding in the lower strain $D3_{Ob}$ event, which only affected grain 2. Consistent with this interpretation, the orientation profiles (Fig. 3H) show that crystal-plasticity and the largest amount of lattice misorientation is recorded parallel to the D3 shortening direction. As the fold grew, the arsenopyrite firstly underwent crystal-plastic deformation, then a fracture propagated through the arsenopyrite in the hinge, perhaps facilitated by embrittlement related to crystal-plastic strain hardening (Fleck et al., 1994). The fracture is infilled with undeformed pyrite (misorientation <2°), again indicating the arsenopyrite crystal-plasticity occurred early during $D3_{Ob}$ microfolding.

We conclude arsenopyrite is remarkably resilient to crystal plasticity at the recorded temperatures of 340° - 460° and pressures of 2 kbars. Two factors likely contribute to this resilience. Arsenopyrite is monoclinic (Bindi et al., 2012), which means only a limited number of slip systems are available for activation. In addition, arsenopyrites are acicular with a strong

shape preferred orientation (SPO). Because there is a competency contrast between arsenopyrite and the quartz-phyllosilicate rich wall rock, at upper greenschist conditions, the SPO allows for accumulation of large strains in the wall rock, while grains aligned with the cleavage remain undeformed (Jessell et al., 2009). We acknowledge that crystal plasticity could be more advanced where arsenopyrites impinge on one another (Barrie et al., 2010), but in this case the percentage of such arsenopyrites was >1% at Obuasi.

Furthermore, our results show B-rims with sharp boundaries cutting primary gold zonation, enriched in As and depleted in Au, but preserving the morphology and crystallographic orientation of the parent arsenopyrite. These relationships are indicators that a pseudomorphic dissolution-reprecipitation reaction (Harlov et al., 2011; Putnis, 2009) has resulted in loss of trace element content (gold) from the crystal lattice. The compositional difference between A- and B-rims indicates that re-equilibration to a more stochiometric composition was the driving force behind the replacement reaction (Geisler et al., 2007).

The texture of the gold zoning in the recrystallized domains of grain 2 (Fig. 3), is blurry and diffuse, in apparent contradiction to the sharp oscillatory zoning of the undeformed domains. This texture can be explained by volume diffusion and migration of dislocations during crystal lattice deformation, i.e. dislocation–impurity pair (DIP) diffusion model (Vukmanovic et al., 2014). Critically, in this same domain, the B-rim gold-poor replacement zones penetrate further (up to three times greater), highlighting a link between crystal-plastic microstructure and facilitation of reaction. We suggest that domains of crystal-plastic microstructure (Fig. 3) increased the porosity along high and low angle crystallographic boundaries (Timms et al., 2012), facilitating the reaction by enhanced mobility of components to and from the reaction front (Fig. 4).

CONCLUSIONS

The implications of our observations for trace element retention and loss in arsenopyrites are profound.

- Arsenopyrite is robust, maintaining its trace element content through conditions of high wall rock strain and metamorphism. This behaviour stands in contrast to other sulphides such as pyrite, characterized by multiple slip systems that can be activated at temperatures as low as 260 °C (Barrie et al., 2011; Reddy and Hough, 2013).
- Such robust properties for arsenopyrite contribute to our understanding of its common association with world-class gold deposits. The ability of arsenopyrite to absorb gold into the crystal lattice and as nanoparticles (Cabri et al., 2000) establishes a clear link with mineralisation. Perhaps more importantly, its ability to maintain such trace element content through high strains means that precious metal resources are then preserved in the rock record. In this manner, arsenopyrite acts like an ark, encapsulating and preserving precious metals or trace elements.
- Figure 4 presents our model of the microstructural response of arsenopyrite to strain, and associated loss of trace elements (gold). Internal deformation only occurs during crenulation of rock fabrics, when arsenopyrites become aligned with the principal contraction direction. Microfolding is accommodated by localised zones of crystal-plastic deformation, strain-hardening and subsequent microfracture. Where crystal-plastic microstructures are developed, they enhance the release of gold from arsenopyrites undergoing reaction back to the natural environment.
- Although the analyses presented here from two arsenopyrites are representative of a large population of arsenopyrites from Obuasi, which we examined petrographically, we recommend future studies of arsenopyrite and other sulphides incorporate EBSD analysis to confirm these results and better understand the role of microstructure in modifying gold deposits.

ACKNOWLEDGMENTS

This study derives from Ph.D. research by DF. AngloGold Ashanti is acknowledged for excellent financial support and field assistance. The Centre for Microscopy, Characterisation & Analysis, University of Western Australia, is funded by the University, State and Commonwealth Governments. SM was funded by the Hammond-Nisbet Endowment.

REFERENCES

Barrie, C. D., Boyle, A. P., Cook, N. J., and Prior, D. J., 2010, Pyrite deformation textures in the massive sulfide ore deposits of the Norwegian Caledonides: Tectonophysics, v. 483, no. 3, p. 269-286.

Barrie, C. D., Pearce, M. A., and Boyle, A. P., 2011, Reconstructing the pyrite deformation mechanism map: Ore Geology Reviews, v. 39, no. 4, p. 265-276.

Bindi, L., Moelo, Y., Léone, P., and Suchaud, M., 2012, Stoichiometric arsenopyrite, FeAsS, from La Roche-Balue Quarry, Loire-Atlantique, France: crystal structure and Mössbauer study: The Canadian Mineralogist, v. 50, no. 2, p. 471-479.

Boyle, A., Prior, D., Banham, M., and Timms, N. E., 1998, Plastic deformation of metamorphic pyrite: new evidence from electron-backscatter diffraction and forescatter orientation-contrast imaging: Mineralium Deposita, v. 34, no. 1, p. 71-81.

Boyle, R., and Jonasson, I. R., 1973, The geochemistry of arsenic and its use as an indicator element in geochemical prospecting: Journal of Geochemical Exploration, v. 2, no. 3, p. 251-296.

Cabri, L. J., Newville, M., Gordon, R. A., Crozier, E. D., Sutton, S. R., McMahon, G., and Jiang, D.-T., 2000, Chemical speciation of gold in arsenopyrite: The Canadian Mineralogist, v. 38, no. 5, p. 1265-1281.

249 Cox, S., 1987, Flow mechanisms in sulphide minerals: Ore Geology Reviews, v. 2, no. 1, p.
250 133-171.
251 Dubé, B., Williamson, K., Mcnicoll, V., Malo, M., Skulski, T., Twomey, T., and Sanborn-
252 Barrie, M., 2004, Timing of Gold Mineralization at Red Lake, Northwestern Ontario,
253 Canada: New Constraints from U-Pb Geochronology at the Goldcorp High-Grade
254 Zone, Red Lake Mine, and the Madsen Mine: Economic Geology, v. 99, no. 8, p.
255 1611-1641.
256 Eilu, P., and Groves, D. I., 2001, Primary alteration and geochemical dispersion haloes of
257 Archaean orogenic gold deposits in the Yilgarn Craton: the pre-weathering scenario:
258 Geochemistry: Exploration, Environment, Analysis, v. 1, no. 3, p. 183-200.
259 Fisher, L. A., Fougerouse, D., Cleverley, J. S., Ryan, C. G., Micklethwaite, S., Halfpenny, A.,
260 Hough, R. M., Gee, M., Paterson, D., and Howard, D. L., 2014, Quantified, multi-
261 scale X-ray fluorescence element mapping using the Maia detector array: application
262 to mineral deposit studies: Mineralium Deposita, p. 1-10.
263 Fleck, N. A., Muller, G. M., Ashby, M. F., and Hutchinson, J. W., 1994, Strain gradient
264 plasticity: Theory and experiment: Acta Metallurgica et Materialia, v. 42, no. 2, p.
265 475-487.
266 Fougerouse, D., Micklethwaite, S., Tomkins, A. G., Mei, Y., Kilburn, M. R., guagliardo, P.,
267 Fisher, L. A., Halfpenny, A., Gee, M., Paterson, D., and Howard, D. L., In press-a,
268 Gold remobilisation and formation of high grade ore shoots driven by dissolution-
269 reprecipitation replacement and Ni substitution into auriferous arsenopyrite
270 Geochimica et Cosmochimica Acta.
271 Fougerouse, D., Micklethwaite, S., Ulrich, S., Miller, J., McCuaig, T. C., Godel, B., and
272 Adams, D., in press-b, Evidence for Two Stages of Mineralization in West Africa's
273 Largest Gold Deposit: Obuasi, Ghana: Economic Geology.

Geisler, T., Schaltegger, U., and Tomaschek, F., 2007, Re-equilibration of zircon in aqueous fluids and melts: Elements, v. 3, no. 1, p. 43-50.

Groves, D. I., Goldfarb, R. J., Gebre-Mariam, M., Hagemann, S., and Robert, F., 1998, Orogenic gold deposits: a proposed classification in the context of their crustal distribution and relationship to other gold deposit types: Ore Geology Reviews, v. 13, no. 1, p. 7-27.

Harlov, D. E., Wirth, R., and Hetherington, C. J., 2011, Fluid-mediated partial alteration in monazite: the role of coupled dissolution–reprecipitation in element redistribution and mass transfer: Contributions to Mineralogy and Petrology, v. 162, no. 2, p. 329-348.

Hirth, G., and Tullis, J., 1992, Dislocation creep regimes in quartz aggregates: Journal of Structural Geology, v. 14, no. 2, p. 145-159.

Jessell, M. W., Bons, P. D., Griera, A., Evans, L. A., and Wilson, C. J., 2009, A tale of two viscosities: Journal of Structural Geology, v. 31, no. 7, p. 719-736.

John, T., Klemd, R., Hirdes, W., and Loh, G., 1999, The metamorphic evolution of the Paleoproterozoic (Birimian) volcanic Ashanti belt (Ghana, West Africa): Precambrian Research, v. 98, no. 1–2, p. 11-30.

Kelly, W. C., and Clark, B. R., 1975, Sulfide deformation studies; III, Experimental deformation of chalcopyrite to 2,000 bars and 500 degrees C: Economic Geology, v. 70, no. 3, p. 431-453.

Le Vaillant, M., Barnes, S. J., Fiorentini, M. L., Miller, J., McCuaig, T. C., and Muccilli, P., 2015, A Hydrothermal Ni-As-PGE Geochemical Halo Around the Miitel Komatiite-Hosted Nickel Sulfide Deposit, Yilgarn Craton, Western Australia: Economic Geology, v. 110, no. 2, p. 505-530.

297 Morelli, R., Creaser, R. A., Seltmann, R., Stuart, F. M., Selby, D., and Graupner, T., 2007,
298 Age and source constraints for the giant Muruntau gold deposit, Uzbekistan, from
299 coupled Re-Os-He isotopes in arsenopyrite: Geology, v. 35, no. 9, p. 795-798.
300 Nolze, G., Winkelmann, A., and Boyle, A. P., 2016, Pattern matching approach to
301 pseudosymmetry problems in electron backscatter diffraction: Ultramicroscopy, v.
302 160, p. 146-154.
303 Oberthür, T., Vetter, U., Davis, D. W., and Amanor, J. A., 1998, Age constraints on gold
304 mineralization and Paleoproterozoic crustal evolution in the Ashanti belt of southern
305 Ghana: Precambrian Research, v. 89, no. 3–4, p. 129-143.
306 Oberthür, T., Vetter, U., Schmidt Mumm, A., Weiser, T., Amanor, J., Gyapong, W., Kumi,
307 R., and Blenkinsop, T., 1994, The Ashanti gold mine at Obuasi, Ghana:
308 Mineralogical, geochemical, stable isotope and fluid inclusion studies on the
309 metallogenesis of the deposit: Geologisches Jahrbuch D, v. 100, p. 31-129.
310 Prior, D. J., Boyle, A. P., Brenker, F., Cheadle, M. C., Day, A., Lopez, G., Peruzzo, L., Potts,
311 G. J., Reddy, S., and Spiess, R., 1999, The application of electron backscatter
312 diffraction and orientation contrast imaging in the SEM to textural problems in rocks:
313 American Mineralogist, v. 84, p. 1741-1759.
314 Putnis, A., 2009, Mineral Replacement Reactions: Reviews in Mineralogy and Geochemistry,
315 v. 70, no. 1, p. 87-124.
316 Ramsay, J., and Huber, M., 1983, The Techniques of Modern Structural Geology, Vol. 1:
317 Strain Analysis Academic Press, London.
318 Reddy, S. M., and Hough, R. M., 2013, Microstructural evolution and trace element mobility
319 in Witwatersrand pyrite: Contributions to Mineralogy and Petrology, v. 166, no. 5, p.
320 1269-1284.

Schwartz, M. O., Oberthür, T., Amanor, J., and Gyapong, W. A., 1992, Fluid inclusion re-equilibration and P-T-X constraints on fluid evolution in the Ashanti gold deposit, Ghana: European Journal of Mineralogy, v. 4, no. 5, p. 1017-1033.

Sung, Y. H., Brugger, J., Ciobanu, C. L., Pring, A., Skinner, W., and Nugus, M., 2009, Invisible gold in arsenian pyrite and arsenopyrite from a multistage Archaean gold deposit: Sunrise Dam, Eastern Goldfields Province, Western Australia: Mineralium Deposita, v. 44, no. 7, p. 765-791.

Timms, N. E., Reddy, S. M., Gerald, J. D. F., Green, L., and Muhling, J. R., 2012, Inclusion-localised crystal-plasticity, dynamic porosity, and fast-diffusion pathway generation in zircon: Journal of Structural Geology, v. 35, p. 78-89.

Urai, J., Means, W., and Lister, G., 1986, Dynamic recrystallization of minerals: Mineral and Rock Deformation: Laboratory Studies: The Paterson Volume, p. 161-199.

Vukmanovic, Z., Reddy, S. M., Godel, B., Barnes, S. J., Fiorentini, M. L., Barnes, S.-J., and Kilburn, M. R., 2014, Relationship between microstructures and grain-scale trace element distribution in komatiite-hosted magmatic sulphide ores: Lithos, v. 184, p. 42-61.

FIGURE CAPTIONS

Figure 1. A) Boudinaged mineralized quartz vein, Obuasi underground mine; B) Micrograph of mineralized metasedimentary ore, comprising gold-bearing arsenopyrites with quartz strain shadows deformed by a crenulation cleavage; C) Schematic of shear strain calculation estimation and equations used in D (modified after Ramsay and Hubert 1983); D) Frequency of shear strain ($e_{stretch}$) calculated from 100 strain shadows surrounding arsenopyrites.

Figure 2. Sample 215-20, grain 1 - the arsenopyrite boundaries, cores and rims are highlighted in red. A) Backscattered electron (BSE) image; B) Cumulative orientation profile along line a-a' (plotted relative to point a) parallel with the arsenopyrite long axis. Only minor crystallographic misorientations are recorded in the grain despite the wall rock being subject to high strain. C) Coloured EBSD maps showing crystallographic misorientations in the range 0-10°. Position of orientation profile a-a' is indicated; D) SIMS elemental gold distribution map. The arsenopyrite is zoned with gold-poor core and gold-rich rim (A-rim).

Figure 3. Sample 215-20, grain 2 - the arsenopyrite boundaries, cores and rims are highlighted in red; A-B) Backscattered electron (BSE) images; C-D) Coloured EBSD maps, showing crystallographic misorientations in the range 0-10° for C and 0-90° for D. Grain 2 coincides with a crenulation microfold and is weakly deformed by this later overprinting low strain event ($D3_{Ob}$), especially in zone D. High-angle boundaries (≥10°) are plotted in black and low-angle boundaries (≥2°) in red. Dynamic recrystallization has produced subgrains and new grains. Position of orientation profiles a-a' and b-b' are indicated; E) SIMS elemental map of ^{197}Au; F) NanoSIMS composite image of ^{197}Au (yellow) and ^{34}S (blue) elemental distribution. B-rims are gold depleted in comparison to A-rims, and are well developed around zone F; G) Pole

figures show the dispersion of orientation data; H) Cumulative orientation profiles (plotted relative to first point) parallel with the long axis (a-a') and short axis (b-b') of grain 2. The largest crystallographic misorientations are recorded along the crystal long axis (a-a'), parallel with the D3 shortening direction.

Figure 4. Interpretation of the microstructural deformation sequence and replacement of arsenopyrite grain 2.

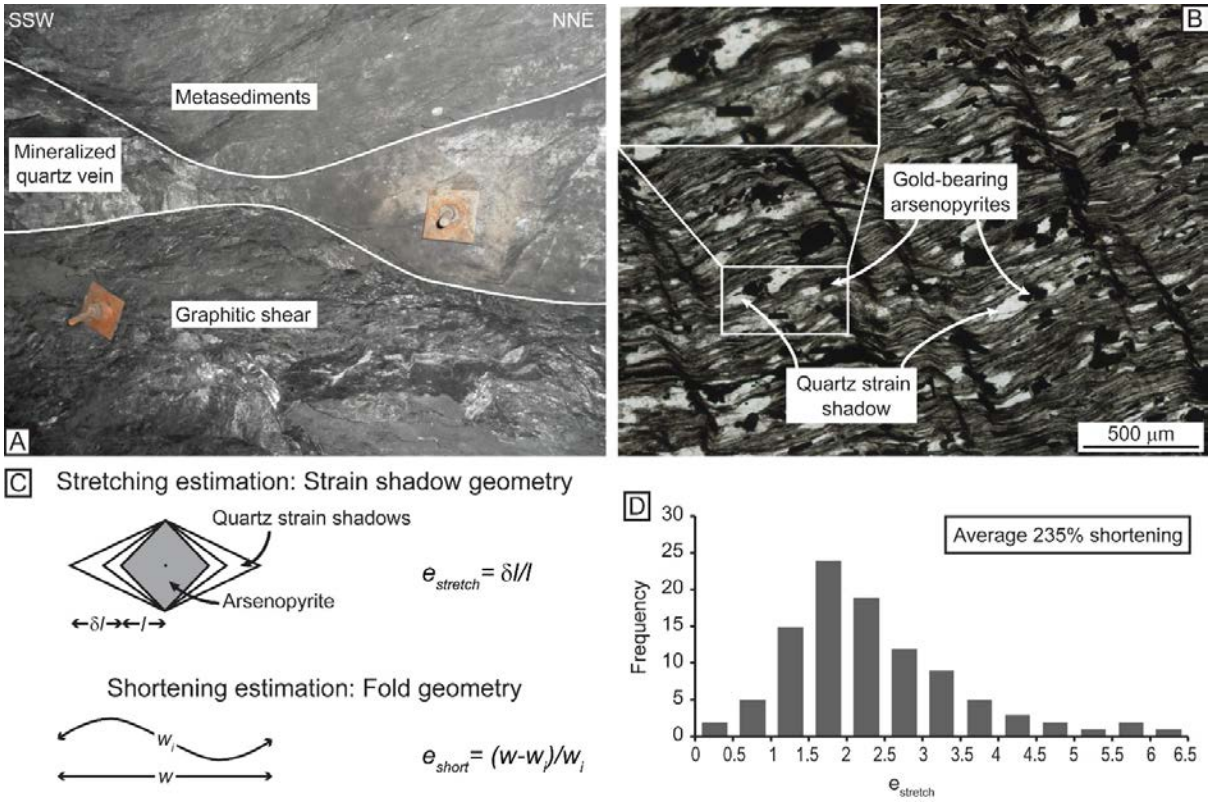
SSW
NNE
Metasediments
Mineralized quartz vein
Graphitic shear
A
B
Gold-bearing arsenopyrites
Quartz strain shadow
500 μm
C
Stretching estimation: Strain shadow geometry
Quartz strain shadows
Arsenopyrite
←δl→←l→
$e_{stretch} = \delta l/l$
Shortening estimation: Fold geometry
w_i
w
$e_{short} = (w-w_i)/w_i$
D
Average 235% shortening
Frequency
0 5 10 15 20 25 30
0 0.5 1 1.5 2 2.5 3 3.5 4 4.5 5 5.5 6 6.5
$e_{stretch}$

370

371

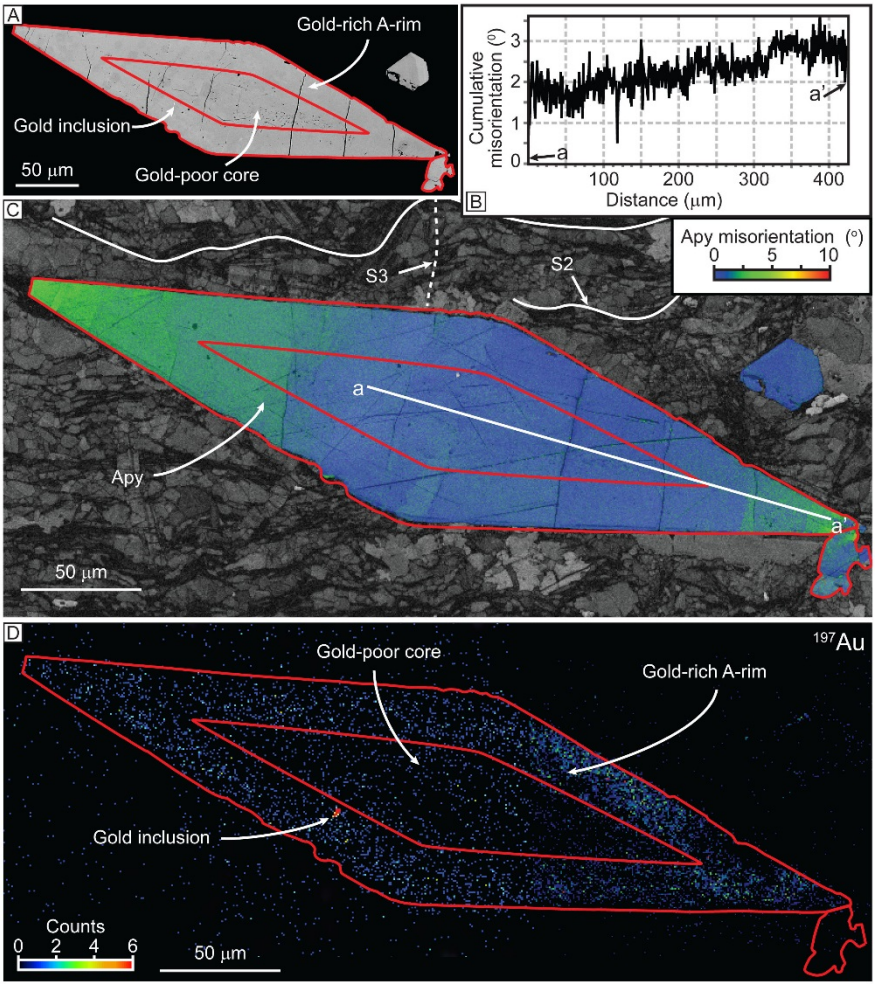
A
Gold-rich A-rim
Gold inclusion
50 μm
Gold-poor core
B
Cumulative misorientation (°)
0
1
2
3
a
a'
100
200
300
400
Distance (μm)
C
S3
S2
Apy misorientation (°)
0
5
10
a
Apy
a'
50 μm
D
197Au
Gold-poor core
Gold-rich A-rim
Gold inclusion
Counts
0
2
4
6
50 μm

372

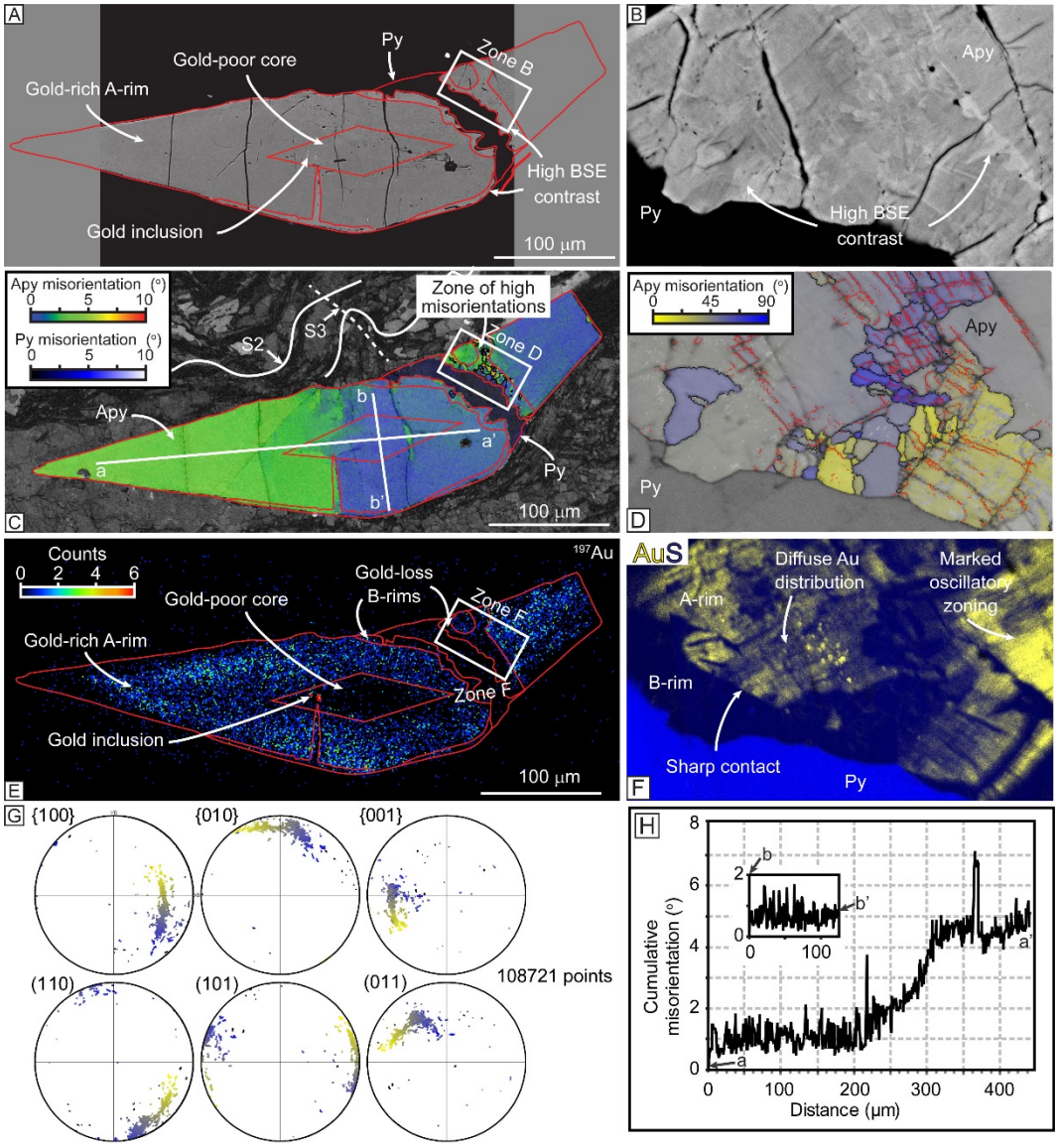
A
Gold-poor core
Py
Zone B
Gold-rich A-rim
High BSE contrast
Gold inclusion
100 μm
B
Apy
Py
High BSE contrast
Apy misorientation (°)
0 5 10
Py misorientation (°)
0 5 10
S2
S3
Zone of high misorientations
Zone D
Apy
b
a'
a
Py
b'
100 μm
C
Apy misorientation (°)
0 45 90
Apy
Py
D
Counts
0 2 4 6
197Au
Gold-poor core
Gold-loss B-rims
Zone F
Gold-rich A-rim
Zone F
Gold inclusion
100 μm
E
AuS
Diffuse Au distribution
Marked oscillatory zoning
A-rim
B-rim
Sharp contact
Py
F
G
{100}
{010}
{001}
(110)
(101)
(011)
108721 points
H
Cumulative misorientation (°)
Distance (μm)
b
b'
a'
a

373

374

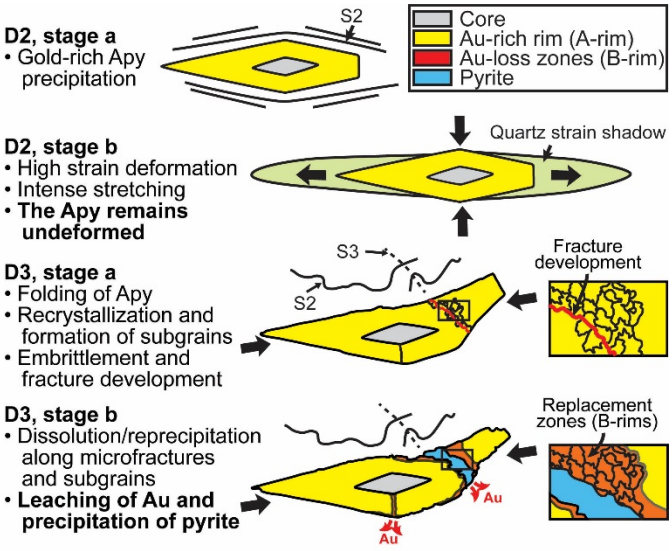
D2, stage a
• Gold-rich Apy precipitation
S2
Core
Au-rich rim (A-rim)
Au-loss zones (B-rim)
Pyrite
Quartz strain shadow
D2, stage b
• High strain deformation
• Intense stretching
• The Apy remains undeformed
S3
S2
Fracture development
D3, stage a
• Folding of Apy
• Recrystallization and formation of subgrains
• Embrittlement and fracture development
Replacement zones (B-rims)
D3, stage b
• Dissolution/reprecipitation along microfractures and subgrains
• Leaching of Au and precipitation of pyrite
Au
Au

375